Critical Mach Number Predictive Methods for Realistic Supersonic Wing / Body Configurations

Noah J Kurus [1]
Timothy T Takahashi [2]
Arizona State University, Tempe, Arizona

and

Ruben E Perez[3]
Royal Military College of Canada, Kingston, Ontario, Canada

This paper outlines the design and validation of a wing designed for a Mach 1.3 cruise supersonic narrow body airliner. The paper will outline how potential flow surface panel models were used to develop the geometry. It will also examine low-speed volume-grid computational fluid dynamics (CFD) solutions for validation as well as present experimental verification in the form of low-speed wind tunnel data along with flow-visualization images. This paper also presents major discrepancies between classical aerodynamic theory and the "reality" of shockwave formation observed in the transonic and supersonic volume gird solutions.

I.   Nomenclature

b	= Wingspan, *ft* full-scale, *in* wind-tunnel-scale
c	= Wing Chord, *ft* full-scale, *in* wind-tunnel-scale
Cp	= Pressure Coefficient
$Cp*$	= Critical Pressure Coefficient
C_L	= Lift Coefficient
L(y)	= Load as a Function of Span, *lbf/ft*
M_∞	= Free Stream Mach Number
M_{crit}	= Critical Mach Number
q	= Dynamic Pressure, *lbf/ft²*
Sref	= Wing Reference Area, *ft²* full-scale, *in²* wind-tunnel-scale
t/c	= Thickness to Chord Ratio
X	= Position Along Chord,
Y	= Position Along Span
Λ	= Leading Edge Sweep,-deg
γ	= Specific Heat Ratio

[1] M.S. Candidate, Aerospace and Mechanical Engineering, School for Engineering of Matter, Transport & Energy, P.O. Box 876106, Tempe, AZ, 85287. Member AIAA.
[2] Professor of Practice, Aerospace and Mechanical Engineering, School for Engineering of Matter, Transport & Energy, P.O. Box 876106, Tempe, AZ, 85287. Associate Fellow AIAA.
[3] Associate Professor, Mechanical and Aerospace Engineering, Royal Military College of Canada, Kingston, ON, K7K 7B4, Canada, Senior Member AIAA.

II.   Introduction

T HIS study highlighting anomalies found in transonic swept wing theory arose from an exercise to design a supersonic civil transport aircraft. The reference aircraft geometry stems from a Senior Capstone Design project [1] at Arizona State University for the Fall of 2019; see FIGURE 1. This design exercise later blossomed into the lead author's Master's Thesis. [2]

The aircraft in question is a 150-seat narrow-body transport aircraft designed to fly daytime flights across the North Atlantic; see FIGURE 2. With a design cruise speed of Mach 1.3, it is fast enough to allow a flyer to 1) take an early morning flight to connect into an east coast hub airport and reach central Europe later that evening or 2) take an early morning flight from a major East Coast gateway city and arrive in the UK or Europe early enough to connect to an evening intra-European flight to their final destination.

With a much lower cruise speed, based around a normal-shock inlet bypass-turbofan cycle, it shares almost no commonality with the Concorde. [3] The proposed design has a large, lightly loaded lambda planform wing and a T-tail. The wing is fitted with leading and trailing edge flaps for take-off and landing. Additional data regarding its general design strategy may be found in our companion paper, AIAA-2011-0591. [4]
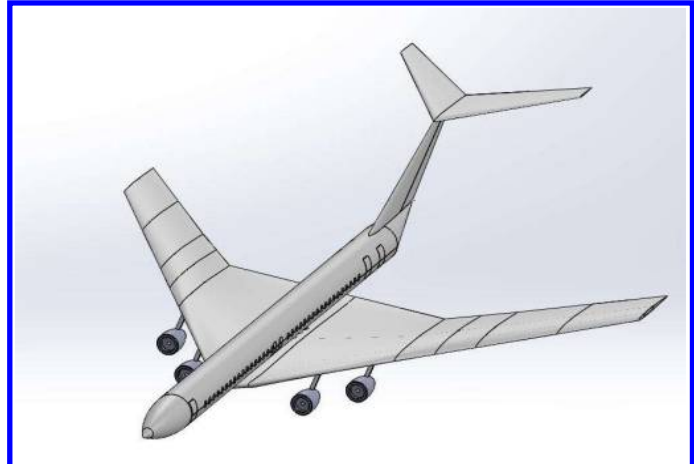

FIGURE 1 – Rendering of Mach 1.3 Supersonic Transport

FIGURE 2 – United Airlines 2019 Transatlantic Route Structure from US East Coast Gateway Airports

Our MDO studies led to a heavy-weight supersonic cruise point near maximum-takeoff-weight (MTOW) at FL400 and M=1.3. Thus, the design CL in supersonic cruise is ~0.21.

Continuing our train of thought from the earlier paper, we will discuss the following elements in this paper:

1. How and why we believe we can use an admittedly simple, potential flow code, to design a supersonic cruise wing.
2. How we can successfully validate our design strategy with a low-speed wind tunnel test.
3. How we can successfully validate our potential flow design against volume-grid CFD at subsonic speeds.
4. Whether we can successfully design a shock-free wing for supersonic flight (as judged by volume-grid CFD solutions).

and

5. Whether we can explain any discrepancies seen in the volume-grid CFD with established theory.

2

III.   Prior Art – The Critical Pressure Coefficient

The critical pressure coefficient is an often-used parameter in which a shape (typically an airfoil) will develop locally sonic flow conditions and will generally trigger the formation of a shock wave. In the case of a finite thickness airfoil immersed in ambient subsonic flow, the flow around the airfoil will inherently produce velocities that are locally faster than the ambient conditions. This effect in turn creates negative pressure coefficients since lower pressures are associated with faster flowing fluid. The goal of this wing design is to maintain a shock-free wing throughout the transonic speed regime, where shocks begin to form just as we reach our design supersonic cruise speed. In theory, to be shock-free, the wing may never develop a pressure coefficient along any part of the planform that is more negative than a Critical Pressure Coefficient, *Cp**. Using a combination of sweep theory and thermodynamic relationships proposed by Küchemann [5], we can postulate target "design point" *Cp**.

A. What is the Critical Pressure Coefficient?

The most conceptually simple approach to the critical pressure coefficient is to look at the case of an infinite wing consisting of a single airfoil profile over its entire infinite span. This setup negates any of the real-world effects that can be expected from a finite length wing with various airfoil profiles as is the case with the wing design in this paper.

To begin with this approach to the critical pressure coefficient, let us first consider the aforementioned purely two-dimensional flow [5]. This lends itself to Equation 1 where the critical pressure coefficient depends only on the free stream Mach number and the specific heat ratio (γ) of the fluid. Referring to FIGURE 3, we see that the critical pressure coefficient trends to 0 as the Mach number trends to 1, and for every Mach number that is less than 1, the critical pressure coefficient gets increasingly negative.

FIGURE 3. Cp^* vs. Mach Number for Purely 2-D Flow

$$C_P^* = \frac{p-p_0}{q} = \frac{2}{\gamma M_\infty^2}\left[\left(\frac{2}{\gamma+1}\right)^{\frac{\gamma}{\gamma-1}}\left(1 + \frac{\gamma-1}{2}M_\infty^2\right)^{\frac{\gamma}{\gamma-1}} - 1\right] \quad (1)$$

B. Busemann's Simple 2-D Sweep Theory

While 2-D simple sweep theory may be sufficient for an ideal infinite span wing, it has does not provide any insight into a wing that is not orthogonal to the incoming flow. In fact, there are benefits to be had in terms of the critical pressure coefficient by sweeping the wing at some angle back from horizontal.

FIGURE 4. Span-wise and Chord-wise Flow Representation on a Swept Wing

The delay in the onset of wing-induced shock-waves, and its resulting drag implications, was first studied in Göttingen, in Germany in the 1930's with the pioneering work of Busemann [6] and Ludweig [7] clearly demonstrated the ability for a swept-back wing to delay shock-wave formation at high, subsonic speeds. R.T. Jones [8,9] expanded on this concept and considered the case an infinite straight wing, albeit at an angle. This forms the basis for simple sweep theory where they then resolve the flow into components parallel and perpendicular to the wing edges as seen in FIGURE 4.

R.T. Jones claims that transverse or span-wise flow components are insignificant; all that matters is the flow component normal to the edges or the chord-wise component. By this extension, they consider the flow essentially 2-D. Simple Sweep Theory notes that the normal component of the flow has an undisturbed velocity equal to the freestream velocity multiplied by the cosine of leading-edge sweep angle ; and the
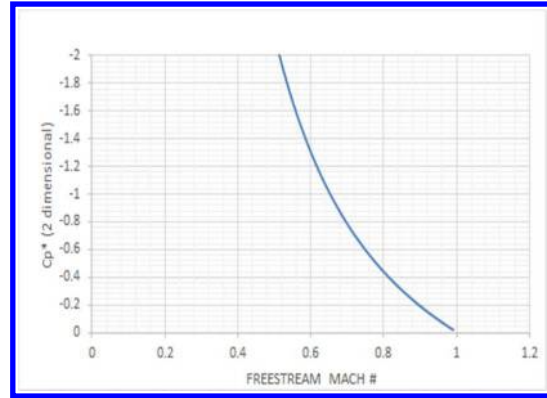
3

'effective' Mach number can be taken as the freestream Mach number multiplied by the cosine of the leading-edge sweep angle (Λ) as seen in Equation 2.

$$Mach_{effectiv} = Mach_{freestream} * \cos(\Lambda) \tag{2}$$

Thus, simple sweep theory claims that if the sweep angle is 60-degrees, then the critical Mach number is doubled since the cosine of 60-degrees is 0.5. This can also be observed graphically in FIGURE 5 where the point at which the effective Mach numbers are reaching sonic are well into the supersonic regime; this intercept is what is referred to as the Critical Mach number in the free stream. By extension, applying the cosine sweep factor to the previous 2-D sweep theory equation leaves us with the operative equation for FIGURE 5 in Equation 3.

$$C_P^* = \frac{p - p_0}{q} = \frac{2}{\gamma \, (M_\infty \cos(\Lambda))^2} \left[\left(\frac{2}{\gamma + 1} \right)^{\frac{\gamma}{\gamma-1}} \left(1 + \frac{\gamma - 1}{2} \, (M_\infty \cos(\Lambda))^2 \right)^{\frac{\gamma}{\gamma-1}} - 1 \right] \tag{3}$$

C. Küchemann Developed an Improved Swept Wing Critical Pressure Equation

Recently, Kirkman & Takahashi [10,11] demonstrated that simple sweep theory is not formally correct. Even for idealized 2-D flow; simple sweep theory predicts significantly inaccurate (and optimistic) performance. They noted that a more nuanced theory, found in Küchemann [5], but stemming from Neumark [12] is correct. As Neumark stated "that the problem of critical Mach numbers for swept wings is a serious scientific problem which cannot be solved by an empirical 'guess' such as, for instance, the notorious" cosine law [12]. The cosine law which he was referring to is the Simple Sweep theory described in the previous section.

Küchemann proposes [5] that the critical pressure coefficient *Cp** for a swept wing is governed by:

$$C_p^* = \frac{2}{\gamma M_\infty^2} \left(\left(\frac{2}{\gamma+1} \right)^{\frac{\gamma}{\gamma-1}} \left(1 + \frac{\lambda-1}{2} (M_\infty \cos(\Lambda))^2 \right)^{\frac{\gamma}{\gamma-1}} - 1 \right) \tag{4}$$

The reader should note that Equation 4 does not require *Cp** to trend to zero when the freestream Mach number reaches 1.0, so long as the wing incorporates sweep. In Küchemann's correct world view, *Cp** reaches zero only when the component of the incipient flow normal to the wing leading edge reaches Mach 1.0 as seen in FIGURE 4. Thus, Küchemann provides a basis to use potential flow methods to develop accurate shock-free supersonic lofts so long as the leading-edge flow remains subsonic [5]; refer to FIGURE 5 as it relates to the critical pressure coefficient for different sweep angles.

However, in the case of this paper, the "sandwich panel" model in our potential-flow code cannot achieve supersonic results and by extension cannot be used to evaluate whether or not the wing is meeting its critical pressure coefficient goal prescribed by Küchemann. Luckily, Küchemann also asserts that for a given wing geometry, the pressure coefficients at different free stream Mach numbers are related by a correction factor equation shown below in Equation 5. In this case the *Cp* on the left side of the equation is the result of Küchemann's improved Equation 4 at Mach 1.25 and the *Cp0* is the corresponding pressure coefficient goal at a low-speed Mach number (Mach 0.3 in this case).
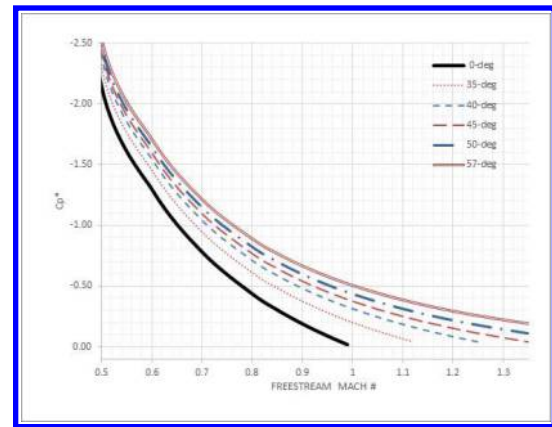

FIGURE 5. Küchemann's Critical Pressure Coefficient for Multiple Sweep Angles
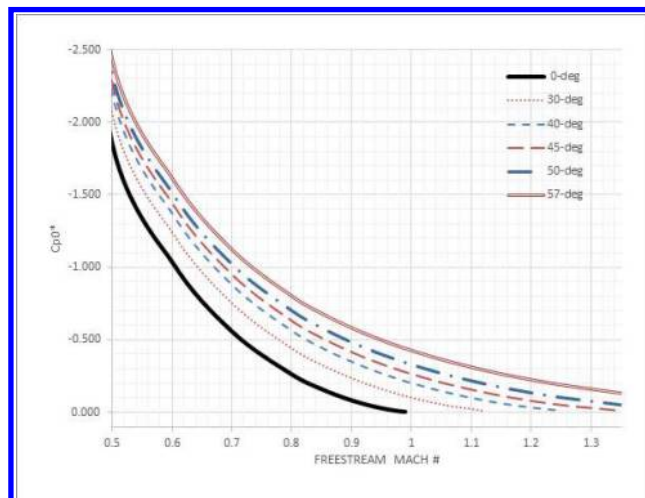
4

FIGURE 6. $Cp0^*$ Workup based on Küchemann's Equation and the Prandtl-Glauert Rule applied to the Mach # normal to the leading edge.
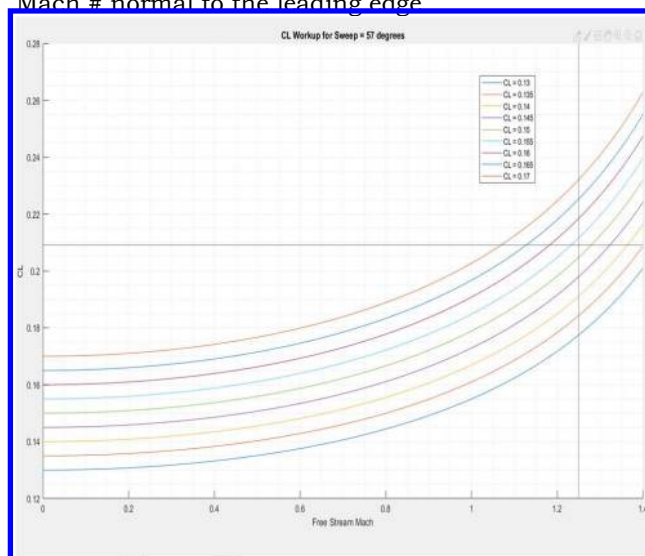

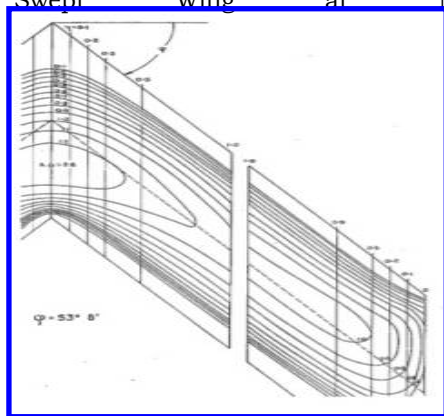FIGURE 7. C_L Workup for a 57-Degree Leading Edge Swept Wing at Mach 1.25

FIGURE 8. Isobars Unsweeping Crossing the Line of Bi-Lateral Symmetry [12]

$$C_p = \frac{c_{p_0}}{\sqrt{1-(M_\infty \cos(\Lambda))^2}} \qquad [5]$$

This procedure was transformed into code and the resultant values for the low-speed-critical pressure at an arbitrary design Mach number are shown in FIGURE 6. Thus, a wing with 57-degrees of leading-edge sweep should have Cp^*=-0.26 when M_∞ = 1.25 and $Cp0^*$ = -0.19 at a sufficiently low subsonic Mach number M_∞ = 0.3. This wing has a clearly subsonic leading edge, M1.25*cos(57°) = M0.68. Hence, if a wing is designed at 57-degrees of sweep it can be expected to develop a pressure profile at low speed where Cp>-0.19, and can further be expected to be shock-free so long as M_∞<1.25.

Another design goal for this wing was the lift characteristics and since the overall lift of a wing is the integration of the net pressures between the upper and lower surfaces over the planform of the wing, lift follows the same sorts of Mach number dependent characteristics. Thus:

$$C_L = \frac{c_{L_0}}{\sqrt{1-(M_\infty \cos(\Lambda))^2}} \qquad [6]$$

This was also transformed into code and the resultant values for the low-speed-critical pressure at an arbitrary design Mach number are shown in FIGURE 7. Thus, a wing with 57-degrees of leading-edge sweep with a design C_L~0.21 at M_∞=1.25 needs to develop C_L~0.15 at low speeds.

D. Upper and Lower Critical Conditions Posed by Neumark

While classic texts [13,14] consider the "wave drag" due to the transonic and supersonic area rule to be independent of the "drag divergence" of a 2-D wing section, the importance of Neumark's [12] rarely cited paper comes to light. Neumark asserts that for any real 3-D wing, that there are both "upper" and "lower" critical conditions. The first is when the local velocity of the flow reached the local sonic condition (this is associated with the concept of the "Lower-Critical-Mach-Number"), and the second, where some component of the velocity (that "normal to the isobars") exceeds a critical condition (this is associated with the concept of the "Upper-Critical-Mach-Number").

For the simple, infinite yawed wing of Busemann [6] it is clear that 'normal to the isobars' means simply 'normal to the leading edge; because there is no plane of bi-lateral symmetry in an infinite wing, hence Busemann's original idea is a particular case of

5

a more general one. From a design perspective, it's preferable to engineer an aerodynamic shape that when pitched to the required angle-of-attack, creates wing-borne isobar patterns that allow the airplane to fly at supersonic speed, while "pretending" to fly at subsonic conditions.

However, since the isobars unsweep as they cross the apex of an ideal wing or cross the fuselage on a practical wing-body configuration (see FIGURE 8), the general criterion also predicts troublesome regions on real airplanes.

While we designed the wing-body to simple swept-wing Küchemann's rules, we realize after-the-fact the wisdom in Neumark's "rules;" he suggests the following strategies to properly utilize Küchemann's equation to support design.

• Center-line region — "Here the isobars cut the section at right-angles, the normal to the isobars coincides with the direction of the flow, and therefore we must reckon with the total velocity of the flow." [12] The crucial point is that with the peak negative value of the unswept isobar contour – it is where "the total velocity reaches its maximum." [12] Following the *Mcr* equation with Λ=0-deg, "conditions for critical Mach number are reached when this velocity at A becomes equal to the local velocity of sound." [12] The key here is an observation that the body of a bi-laterally symmetric airframe will **always** generate shock waves at freestream Mach numbers < 1; these shock waves may then "contaminate" the flow over the rest of the wing.

• Mid-span – For "section(s) at a considerable distance from both the kink and the tip …. the flow here is almost identical with that on an infinite sheared wing." [12] "Only the maximum velocity component normal to the isobars (i.e., normal to wing edges) must be taken into account … the relevant Mach number may be considered as upper critical." [12] Thus, the *upper Mcr* will be that predicted where Λ equals either the leading-edge wing sweep or the sweep angle of the **peak negative value swept isobar contour**. Note that, with large sweep angles, "the upper critical [Mach number] may, of course, exceed 1." [12]

TABLE 1 – *Cp** as a function of Mach#
  and sweep (Eqn [4])

MACH #	CP* no-sweep (i.e. LCM)	25	30	35	40	45	50	57
0.3	-6.95	-7.0	-7.1	-7.1	-7.2	-7.2	-7.3	-7.3
0.5	-2.13	-2.2	-2.3	-2.3	-2.4	-2.4	-2.5	-2.5
0.6	-1.29	-1.4	-1.4	-1.5	-1.5	-1.6	-1.6	-1.7
0.7	-0.78	-0.90	-0.94	-0.99	-1.04	-1.09	-1.15	-1.21
0.8	-0.43	-0.56	-0.61	-0.66	-0.71	-0.77	-0.82	-0.89
0.85	-0.30	-0.43	-0.48	-0.53	-0.59	-0.64	-0.70	-0.77
0.86	-0.28	-0.41	-0.46	-0.51	-0.57	-0.62	-0.68	-0.75
0.87	-0.25	-0.38	-0.43	-0.49	-0.54	-0.60	-0.65	-0.72
0.88	-0.23	-0.36	-0.41	-0.47	-0.52	-0.58	-0.63	-0.70
0.89	-0.21	-0.34	-0.39	-0.45	-0.50	-0.56	-0.61	-0.68
0.9	-0.19	-0.32	-0.37	-0.43	-0.48	-0.54	-0.59	-0.67
0.91	-0.17	-0.30	-0.35	-0.41	-0.46	-0.52	-0.58	-0.65
0.92	-0.15	-0.28	-0.33	-0.39	-0.45	-0.50	-0.56	-0.63
0.93	-0.13	-0.26	-0.31	-0.37	-0.43	-0.49	-0.54	-0.61
0.94	-0.11	-0.24	-0.30	-0.35	-0.41	-0.47	-0.52	-0.60
0.95	-0.09	-0.23	-0.28	-0.34	-0.39	-0.45	-0.51	-0.58
0.96	-0.07	-0.21	-0.26	-0.32	-0.38	-0.44	-0.49	-0.56
0.97	-0.05	-0.19	-0.25	-0.30	-0.36	-0.42	-0.48	-0.55
0.98	-0.03	-0.18	-0.23	-0.29	-0.35	-0.40	-0.46	-0.53
0.99	-0.02	-0.16	-0.21	-0.27	-0.33	-0.39	-0.45	-0.52
1.05		-0.07	-0.13	-0.19	-0.25	-0.31	-0.37	-0.44
1.1		0.00	-0.06	-0.12	-0.19	-0.25	-0.31	-0.39
1.2				-0.02	-0.09	-0.15	-0.22	-0.29
1.25					-0.04	-0.11	-0.18	-0.26
1.3					0.00	-0.07	-0.14	-0.22

TABLE 2 – *Cp0** to Critical Mach#
  Küchemann corrected by Prandtl-Glauert (Eqn [4 & 5])

CRITICAL MACH #	CP0* no-sweep (i.e. LCM)	25	30	35	40	45	50	57
0.3	-6.627	-6.78	-6.84	-6.91	-6.98	-7.06	-7.13	-7.23
0.5	-1.848	-2.00	-2.06	-2.12	-2.19	-2.27	-2.34	-2.44
0.6	-1.035	-1.18	-1.24	-1.30	-1.37	-1.44	-1.52	-1.62
0.7	-0.556	-0.69	-0.75	-0.81	-0.88	-0.95	-1.02	-1.12
0.8	-0.261	-0.38	-0.44	-0.50	-0.56	-0.63	-0.70	-0.80
0.85	-0.159	-0.27	-0.32	-0.38	-0.45	-0.51	-0.58	-0.68
0.86	-0.142	-0.26	-0.30	-0.36	-0.43	-0.49	-0.56	-0.66
0.87	-0.125	-0.24	-0.29	-0.34	-0.41	-0.47	-0.54	-0.64
0.88	-0.110	-0.22	-0.27	-0.32	-0.39	-0.45	-0.52	-0.62
0.89	-0.095	-0.20	-0.25	-0.31	-0.37	-0.43	-0.50	-0.60
0.9	-0.082	-0.19	-0.23	-0.29	-0.35	-0.42	-0.49	-0.58
0.91	-0.069	-0.17	-0.22	-0.27	-0.33	-0.40	-0.47	-0.56
0.92	-0.057	-0.16	-0.20	-0.26	-0.32	-0.38	-0.45	-0.54
0.93	-0.047	-0.14	-0.19	-0.24	-0.30	-0.37	-0.43	-0.53
0.94	-0.037	-0.13	-0.17	-0.22	-0.28	-0.35	-0.42	-0.51
0.95	-0.028	-0.12	-0.16	-0.21	-0.27	-0.33	-0.40	-0.50
0.96	-0.020	-0.10	-0.15	-0.20	-0.26	-0.32	-0.39	-0.48
0.97	-0.013	-0.09	-0.13	-0.18	-0.24	-0.31	-0.37	-0.47
0.98	-0.007	-0.08	-0.12	-0.17	-0.23	-0.29	-0.36	-0.45
0.99	-0.002	-0.07	-0.11	-0.16	-0.22	-0.28	-0.34	-0.44
1.05		-0.02	-0.05	-0.10	-0.15	-0.21	-0.27	-0.36
1.1			-0.02	-0.05	-0.10	-0.16	-0.22	-0.31
1.2				0.00	-0.03	-0.08	-0.14	-0.22
1.25					-0.01	-0.05	-0.10	-0.19
1.3						-0.03	-0.08	-0.16

6

• Tip section — Here it is likely that "the isobars bend sharply in the tip area to run nearly parallel to the flow." [12] In other words, the sweep of the isobars reaches 90-degrees. Thus, "the critical conditions are reached here much later than in the central kink, and apparently also later than in the regular region." [3] Thus, there is little reason to dwell on the concept of "a 'tip critical Mach number '." [12]

Thus, to support design, we should compute the Cp^* from Küchemann's equation [5] at a variety of sweep angles – from zero (to help estimate the Lower-Critical-Mach-Number) through the leading-edge sweep angle to consider highly swept isobar lines. Reviewing TABLEs 1 and 2, we see Cp^* estimates made as a function of freestream Mach number and the relevant sweep angle both in terms of the Cp^* at a given freestream Mach number and a $Cp0^*$ ("corrected back to Mach 0") relating to an estimated low-speed $Cp0$ value which will develop an incipient shock wave at an elevated freestream flight speed.

E. Incompressible Panel Method Code Used as the Basis for Design

To solve the velocity distribution over the surface of the airplane, and determine the basic super-velocity field, the "sandwich panel" feature in *VORLAX* is used to support the design process. *VORLAX* [15] is a generalized subsonic/supersonic vortex lattice panel method code. While the code supports subsonic and supersonic influence coefficients for thin, "double-impermeable" panels (conventional "vortex lattice" paneling), it only supports subsonic solutions using the "single-impermeable" panel elements needed to properly model a thick, cambered wing. In addition, the generalized vortex lattice method

FIGURE 9. Flow Structure Around *VORLAX* Sandwich Panels

is a potential flow model and hence lacks any ability to model shock waves. A visual for how the sandwich panels work in provided in FIGURE 9 where the velocity normal to the surface is zero on the outside of the panels but unknown on the inside. Since they are both single-impermeable, as with any vortex lattice code, the velocity on the inside does not affect the solution and the normal velocity on the outside is zero.
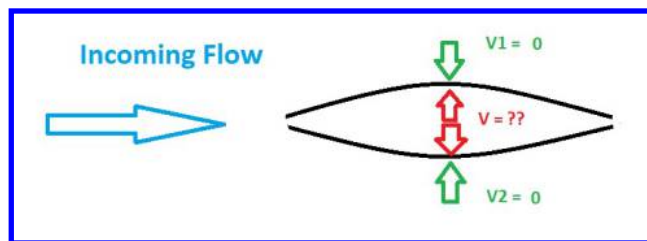
Nonetheless, it is easy to build and solve thick sandwich panel models using this code, and hence its utility will be showcased to design a subcritical or slightly supercritical supersonic wing using it.

Since a *VORLAX* "thick sandwich" panel model is constrained to run at only subsonic Mach numbers, it is possible to predict surface pressures that would otherwise form shockwaves. Thus, the trust range of *VORLAX* includes almost any geometry so long as the predicted pressures due not exceed the shockwave producing critical pressure coefficient for a swept, finite wing. This trustworthiness condition poses no issues to this design since the overall goal is to design a wing that never reaches its critical pressure coefficient levels in the first place.

IV. Reference Geometry

The reference geometry used in this paper was developed using *VORLAX* as the panel-method solver. The design process is covered in greater detail in AIAA 2021-0591. [4]

To summarize the wing geometry:
- Is optimized for Mach~1.25 cruise; CL = 0.21 @ M=1.25
- Should have a nearly elliptical transverse loading distribution at this condition; minimizing induced drag.
- Should not develop strong shock waves at cruise conditions.
  - Ensuring that the critical Mach number is just below the cruise speed of Mach 1.3; Mach~1.25.
  - Ensuring that local pressure coefficients do not exceed the critical pressure coefficient.
- The wing must develop favorable stall conditions.
  - The root of the wing needs to stall first as to maintain controllability and create a nose down pitching moment.

- - The aircraft must maintain control power on its wing mounted control surfaces at the onset of a stall.
- Pressure isobars must line up consistently with the leading-edge sweep of the wing.
  - Non-aligned isobars work adversely to the effects of sweep.

A. Developing the Geometry

The geometry was developed in such a way that the resultant wing features airfoils that are negatively cambered near the side of body in a "reflex camber" fashion to help improve pressure isobar alignment over the span of the wing. As we transition out to the wing tips the airfoils exhibit positive camber. To counteract the effects of camber on lift (recall negative camber produces significantly less positive lift) there is great attention paid to the twist of the wing along its span. At the root the wing is twisted in a "leading edge up" fashion but this decrease going out on the span and by the wing tips the wing is twisted slightly "leading-edge-down". For better visualizations of the airfoils, airfoil pressure distributions, and geometry parameters over the span see "Aerodynamic Design Challenges of a Mach 1.3 Supersonic Airliner Concept" [4].

How did we develop this final shape? We use an iterative process where we define the wing in terms of 6 basis airfoils, each of which have an associated thickness (t/c), camber (% camber) and local incidence (twist). Thus, we pose the wing design problem in terms of 18 independent variables. The airfoil shape is made up of scaled thickness forms modified by a scaled camber line. The basic thickness profiles (the NACA 64 and 65) control the location of the maximum thickness – otherwise they are very similar. These thickness forms were then scaled up or down as desired. The final lofting airfoils impose a camber line upon the basic thickness form. We chose NACA 62, 63 and 64 cambers lines as possible reference. We could then scale these camber lines in order to impose more or less leading-edge droop as necessary. We can see that all of our basis camber lines feature the majority of their camber towards the front of the airfoil. The geometry we developed therefore is a prismatic loft between each of the six defining airfoil sections.

Some of the logic behind a few design characteristics is not immediately apparent. For example, the overall thickness distribution of the airfoils is a byproduct of the drag estimation tool being limited to a maximum average thickness. Additionally, one might wonder why there is such a large chord extension (Yehudi) near the side of body. This comes as a byproduct of landing gear fitment on a fully configured airplane prototype, once again looking at this from a practical point of view [1]. We can see the overall loft as rendered and ready for wing-body CFD and wind tunnel testing in FIGURE 10.
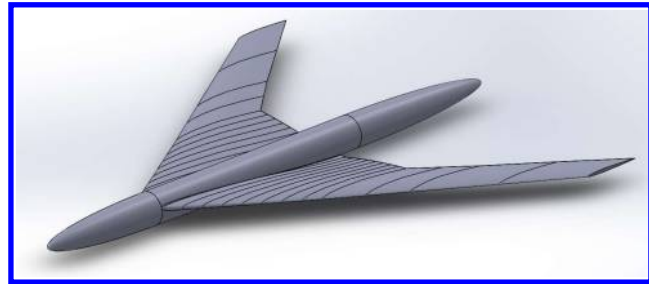

FIGURE 10 – OVERALL WING/BODY GEOMETRY

B. Design Point Implemented as a Low-Speed Design Solution

The overall wing design as constructed in *VORLAX* produces low speed results which satisfied our initial design goals. For lift, we wanted to achieve *CL*=0.153 @ *M*=0.3; our final geometry achieved *CL*=0.15 at α=0.2-deg. At the time of design, we targeted a low-speed suction goal for *Cpmin* > -0.315. We realize on reflection that our original computation of *Cp0** used the free-stream Mach number rather than the sweep corrected normal-to-the-leading edge Mach number (our proper goal should be for *Cpmin* > -0.19).   Our converged *VORLAX* design exceeded our original *Cpmin* goals, with a low speed *Cpmin*=-0.229; this reflects an anticipated Upper-Critical-Mach-Number of *M*~1.2 (only a slight shortfall).

See FIGURE 11 for the pressure coefficient contour for the upper surface of the wing. The lower surface isobar is not shown but the pressure coefficients on this surface are much less negative that the top surface.

This geometry achieves the key lift and pressure goals, but this design also accomplishes all of the nominal wing goals prescribed by Obert [16] and Neumark [12]. FIGURE 12 shows that the loading of the wing is very nearly elliptical with only about a 2.4% deviation from ideal. Induced drag losses from a loading of this type would likely only be incrementally larger than a perfectly loaded wing.

Additionally, the pressure isobar alignment for strong negative suctions (i.e. $Cp<<0$) is very consistent with the leading-edge sweep of the wing which has several positive design goal implications. First, the wing should not suffer any of the wave drag penalties that come from non-aligned isobars described by Neumark [12]. Plus, the critical conditions described in this work should be very consistent with Neumark's definition of the "upper" critical conditions due to the similarity of the isobar sweep (see FIGURE 13) and the geometrical sweep of the wing and at higher speeds this pattern should cause the shock to first form near the leading edge. The pressure profiles are a byproduct of the twist, camber, and thickness strategies.

The reflex camber near the side of body should help stall characteristics. A swept wing will exhibit favorable stall behavior if the root of the wing were to stall first. The reason for this is simple, the root of the wing is ahead of the moment-reference-point. By stalling the only part of the wing where the local airfoil inherently produces a nose up pitching moment (see negative camber) it leaves only airfoils producing a nose down pitching moment (see positive camber) which is a stable configuration. Since the *VORLAX* solution cannot directly capture stall, we cannot see any supporting evidence in *VORLAX* solutions, but we will examine stall characteristics in the associated wind tunnel test.
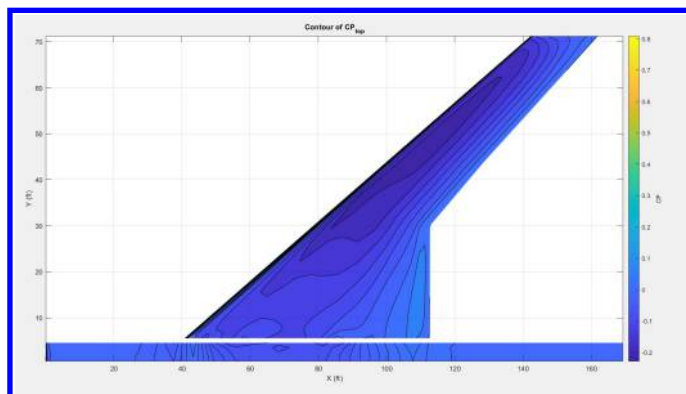
FIGURE 11: Upper Surface ISOBAR contours from the low speed *VORLAX* solution.
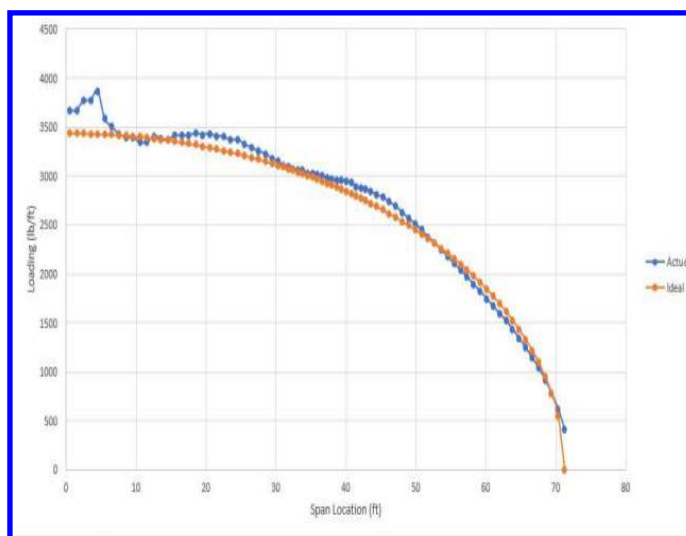
FIGURE 12: Transverse Span Load From Low-Speed Design Solution
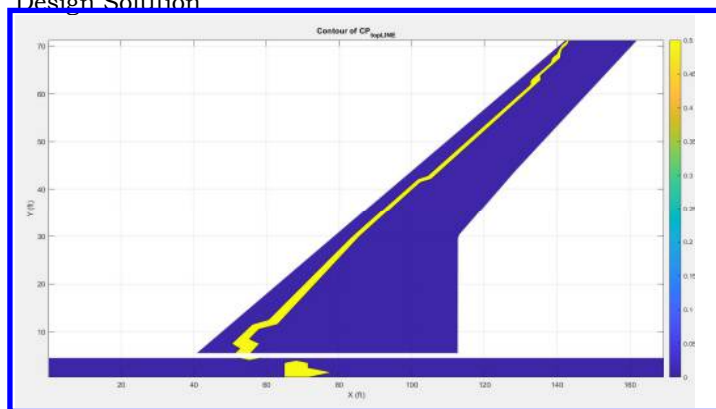
FIGURE 13: color scale enhanced upper surface ISOBARs – to highlight line of peak underpressure

9

V. Low Speed Results

A. Wind Tunnel Procedure

We collected experimental data in the closed-circuit wind tunnel at Royal Military College (RMC) of Canada in Kingston, Ontario; see FIGURE 14. The wind tunnel has a 0.76m x 1.08m (42" x 30") test section and is capable of producing free stream airspeeds up to 60 m/s, with a turbulence intensity of 0.16% [17] The tunnel measures freestream flow speed using a pitot static probe connected to an Omega PX164 manometer. Forces and moments were measured using a six-axis ATI Industrial Nano-25 force-torque balance. Velocity uncertainty was calculated to be 0.05 m/s at our 25 m/s test speed (M=~0.075, q=8.0 lbf/ft^2, ~48-KEAS) while maximum force and moments resolution were calculated to be 1/48 N and 1/1320 N-m respectively. The Unit Reynolds Number at 25-m/sec is ~525,000/ft.

Given the dimensions of the 1:72 scale model (see TABLE 1), the maximum blockage at the maximum tested angle of attack of 22-deg would be approximately 9%. Normal tests would occur at blockage ratios significantly lower than the 10% at which Pope & Harper recommend using blockage corrections., [18] The streamwise Re# on the reference chord is ~230,000.

We fabricated the wind tunnel model from acrylonitrile styrene acrylate (ASA) plastic using a high definition Fortus 450 production 3D printer with a dimensional tolerance of the manufacturing process of 0.3 mm. Using a Mitutoyo SJ-400 surface roughness tester, we determined the surface finish of the model as smooth to 1.5+/-0.2 μM. The surface roughness of the model (since we did not sand the model) trips the BL making the measurements close to fully turbulent.

We collected force and moment data and performed flow visualization at the maximum speed allowed by the model structure: 25 m/s. Angles between -5-deg and 22-deg were measured, low angles up to 8-deg were set to capture initial flow separation and higher angles measured the effects of vortex-lift. Flow behavior was also observed via tufts and oil-flow visualization.

The RMC team precisely took wind-off tare measurements to correct for model weight effects.

B. *SU2* Procedure

The same model that was presented in FIGURE 10 was gridded up sufficiently well such that it could be run through *SU2* (version 7.0 on Windows) at various Mach numbers, both high and low. In modern CFD software, there are a vast number of solvers that can be employed to solve the flow field, all coming with their own benefits and drawbacks. In this case, an Euler solver was chosen, which is a considerably robust and computationally efficient

FIGURE 14: Installation at RMC

TABLE 1 – Wind Tunnel Model Dimensions

Trapezoidal Planform Area - Reference Area	124.52 in^2
Wingspan – Reference Span	23.9 in
Mean Geometric Chord – Reference Chord	5.2 in
Fuselage Length	28.22 in (from nose tip to tail
Fuselage Diameter	1.68 in
Leading Edge Sweep	57.1-deg
Root Chord	7.00 in
Tip Chord	3.26 in
Aspect Ratio	4.596
Taper Ratio	0.465
Wing-Body Junction Frame Station	6.67 in (aft of tip of nose on the model)
Moment Reference Point Frame Station	8 in (aft of wing body junction) 14.66 in (aft of tip of nose cone)

10

method of solving the flow field. In an ideal world where we had unlimited computing power at our disposal, more intricate and rigorous programs such as RANS or LES would have beneficial, unfortunately this was not the case. However, the Euler solver and gridding scheme that was utilized for these trials is more than sufficient for the level of resolution and precision being sought after in the flow field. Additionally, the Euler solver is an inviscid code which is consistent with the *VORLAX* code. Additionally, this analysis required nearly 40 different runs of *SU2*, each taking about 6 hours to complete, so if these had been done with a RANS or LES solver, the time constraint would not have been realistic for the scope of this work.

Before going into detail about any of the results, we must be certain the grid density of the model is sufficient to capture the intricacies of shock formation and wing isobar patterns. However, the computing power that was at our disposal was not incredibly powerful, so the number of total cells needed to be kept below about 30 million (1 million cells ~ 1 GB of RAM). FIGURE 15 shows screenshots of the volume grid that were used and we can observe that the grid captures the curvature of the body quite well. Note that the model is symmetric, thus saving a bit of computational cost. The overall grid setup was validated via a grid convergence study as well for optimal results.

C. Low Speed Force & Moment Results Demonstrate Broad Agreement

The first thing we notice from the low-speed results is the similarity of the isobars presented in FIGURE 16. We can clearly see that the overall isobar pattern is very similar, and the magnitudes of the pressure coefficients generally line up on the top surface. At this point we can deduce that the low-speed results from the inviscid potential flow code (*VORLAX*) are valid in comparison with the more complex inviscid Euler solver in *SU2*. These contours are remarkably close to one another giving us confidence in the possibilities of the potential-flow design process.

The peak negative *Cp* around the wing-body junction where the isobars unsweep is *Cpmin* ~-0.1; around the 2/3 exposed chord point at the wing/body junction. We see this in both the *SU2* and the *VORLAX* solution. Following Neumark's rules, we would enter TABLE 2 with *Cp0*=-0.1 to estimate the Lower-Critical-Mach-Number to be *M*~0.89.

We can also confirm that the *SU2* result produces *Cpmin* ~ -0.27 aligned roughly with the leading edge. Entering TABLE 2 with *Cp0*=-0.27 and a Λ=57-deg we would estimate the Upper-Critical-Mach-Number to be *M*~1.15.
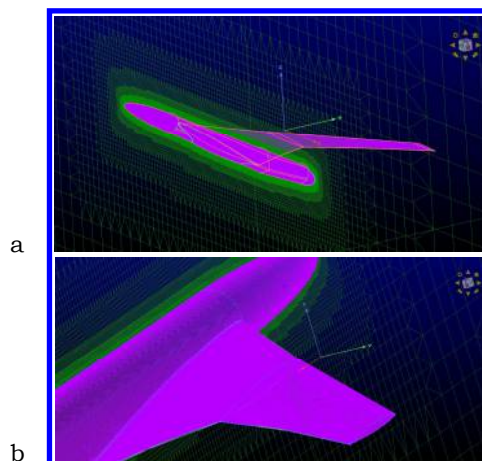

a
b

FIGURE 15: Grid Density Screenshot for the *SU2* Model. A) Volume Grid. B) Surface Grid
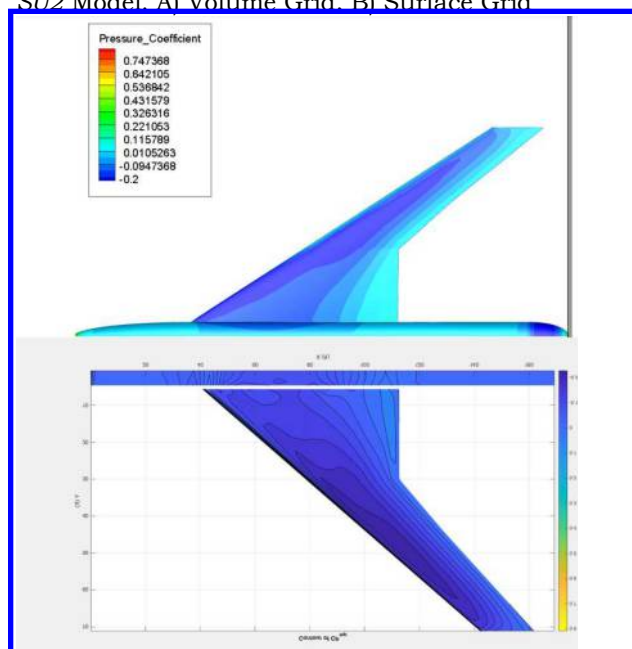
FIGURE 16: Low Speed Comparison Between *SU2* (Top) and *VORLAX* (Bottom) (M = 0.3, α = 0.2-deg)

We can also compare overall force and moment data estimated using *VORLAX* with the *SU2* solutions.

From FIGURE 17, we can see that the lift coefficient verses α correlation from the wind tunnel closely agrees with both the *SU2* solutions and both flat plate and cambered "sandwich" panel *VORLAX* solutions. The wind tunnel data reveals a complete lack of a classical "stall break;" further work both quantitative and

11

qualitative demonstrates that the wing has an initial stall at α~6-deg, followed by vortex lift recovery. Refer to Section D for flow visualization.

We next turn to FIGURE 18, a plot of *CL* vs *(CD-CD0)*. Since *VORLAX* is purely inviscid, a flat-plate model inherently has zero drag at zero lift. The *SU2* solutions, due to the nature of pressure integration (including the forebody but truncating the aft fuselage closeout) do exhibit zero-lift drag (from axial pressures) despite their inviscid nature. Finally, the RMC wind tunnel data inherently captures viscous skin-friction effects. To best compare these diverse datasets, we normalize each data set by referencing all lines and symbols to the zero-lift-drag of the individual source. We see here that the RMC wind tunnel data closely matches the *SU2* solution for *CL*<0.4; at higher angles of attack (α>6-deg) the wind tunnel records higher drag than does *SU2*; this is consistent with observations of separated flow shown in Section D.
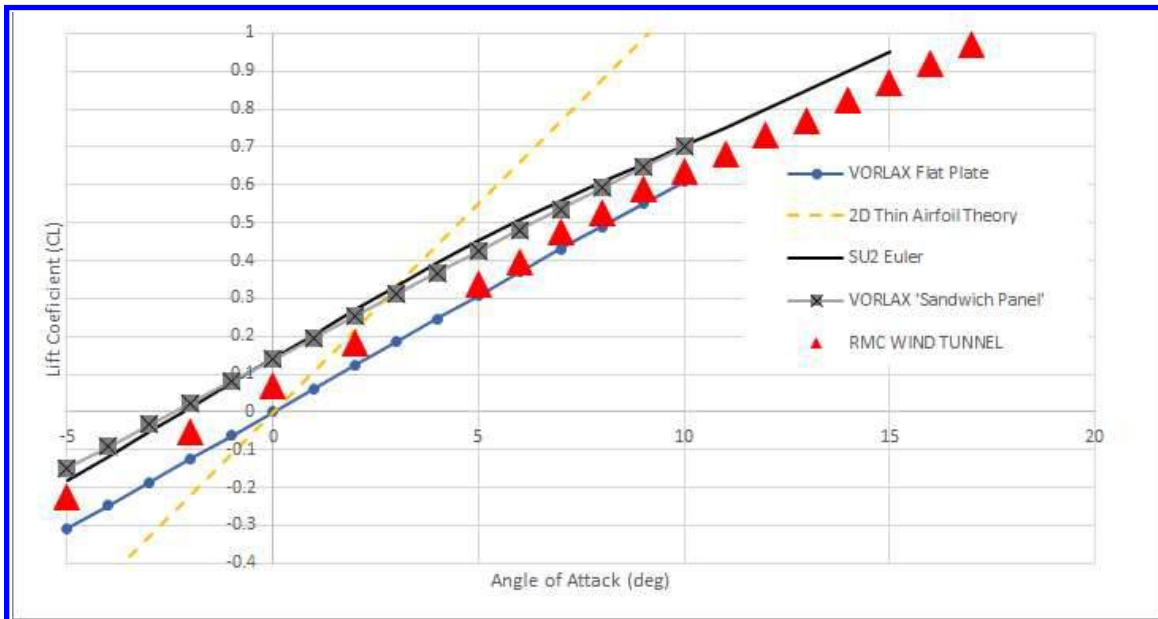
FIGURE 17. *CL* vs. α Plot for the Low-Speed Case with *VORLAX*, Wind Tunnel and *SU2*
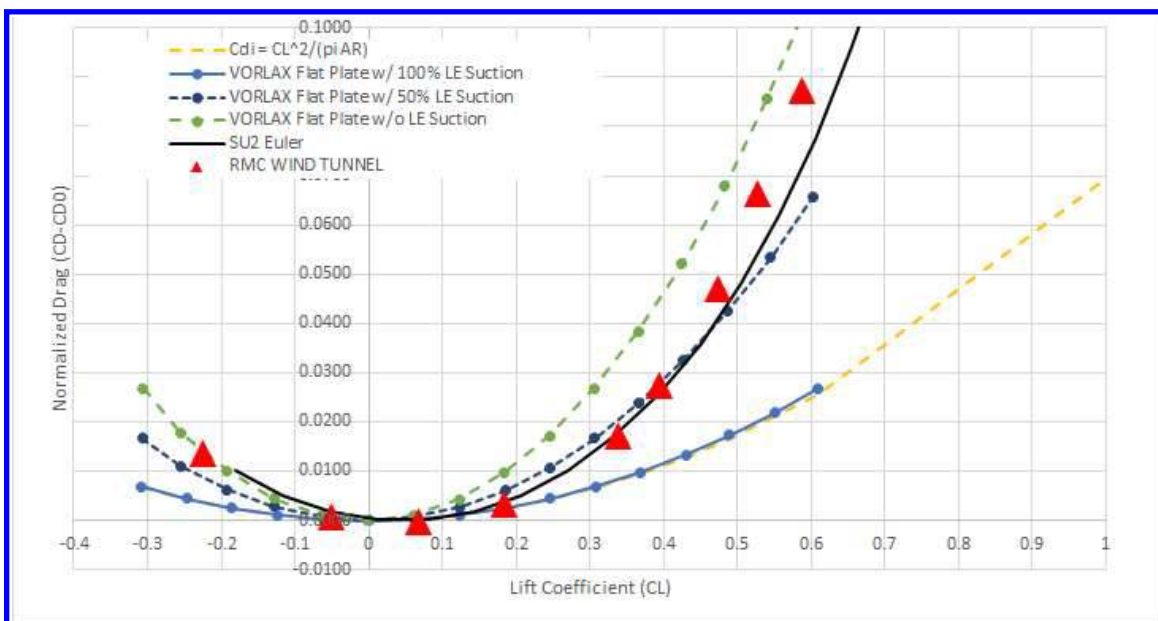
FIGURE 18. *CL vs. CD -CD0* Plot for the Low-Speed Case with *VORLAX*, Wind Tunnel and *SU2*

12

© 2021 –NJ Kurus & TT Takahashi & RE Perez

In terms of the *VORLAX* solutions, the flat panel model with full analytical leading-edge-suction (a typical setting for a wing like this with a classical NACA blunt-leading-edge airfoil) closely matches the expected $CL^2/\pi AR$ parabola. Neither *SU2* nor RMC wind tunnel matches this; they both exhibit markedly higher drag-due-to-lift at $CL>\sim 0.2$. We see here that both Euler and Wind Tunnel closely match a *VORLAX* solution with 50% analytical leading-edge-suction. If we run *VORLAX* without any leading-edge-suction, modelling a wing with thin, sharp leading-edges, it predicts higher drag yet. We will show in Section VI that once we "calibrated" *VORLAX* with the 50% analytical leading-edge-suction correction, it predicts the *CL* vs *CD* trends the geometry exhibits at transonic and supersonic speeds.
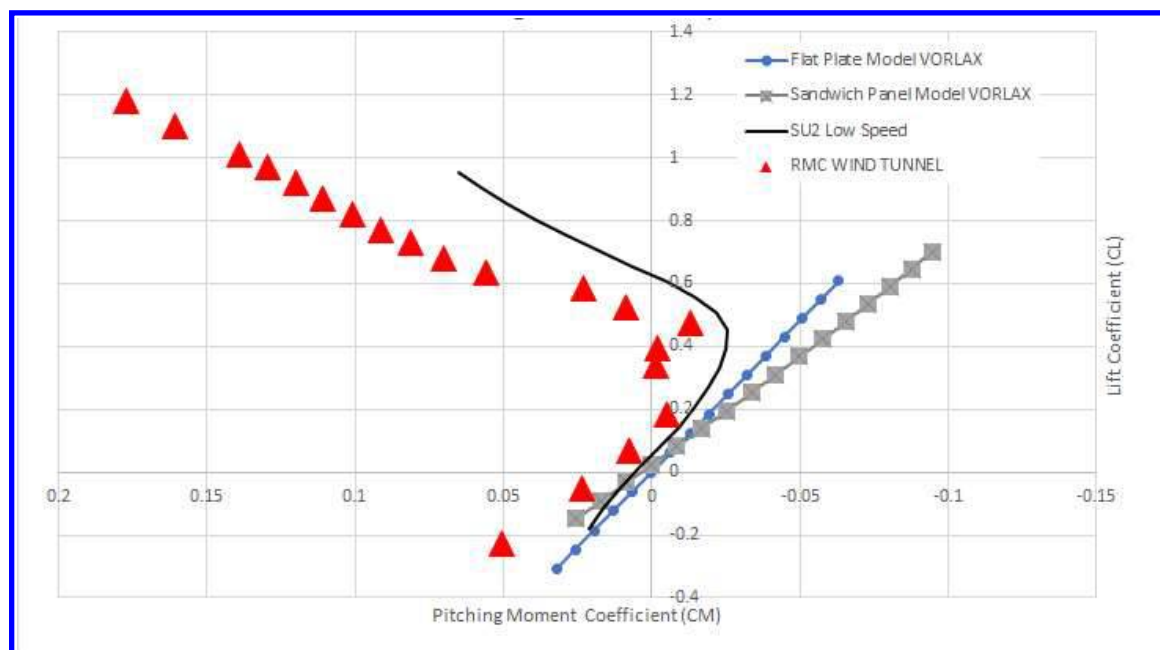
FIGURE 19. C_M *vs.* C_L Plot for the Low-Speed Case with *VORLAX*, Wind Tunnel and *SU2*

Lastly, we examine the wing/body ensemble pitch stability in FIGURE 18. We see that moments are similarly in close agreement between Wind Tunnel, *SU2* model and *VORLAX* in the linear region of the plot corresponding to angles of attack between -3-deg and +3-deg. Both *SU2* and Wind Tunnel show a strong break in stability (transitioning from ~15% stable to ~20% unstable) occurring around $CL\sim 0.4$ (α=6-deg).

Recall that this plot represents the low-speed performance of the supersonic cruise geometry used to explore and validate the potential flow design process. Although we observe the sharp break in longitudinal stability around $CL\sim 0.4$ (α=6-deg), we are mainly concerned with the operating conditions of $CL\sim 0.153$ (α=0.2-deg). Plus, the stability characteristics of this airplane would be enhanced greatly with the addition of a properly sized VT and HT which the CFD and wind tunnel models lack. As this aircraft was envisioned to incorporate a high-lift-system it clearly needs a leading-edge device on the outboard wing to modify the pitch break presently created by the loss of lift at the aft swept wingtips.

13

FIGURE 20 – 2-deg AOA

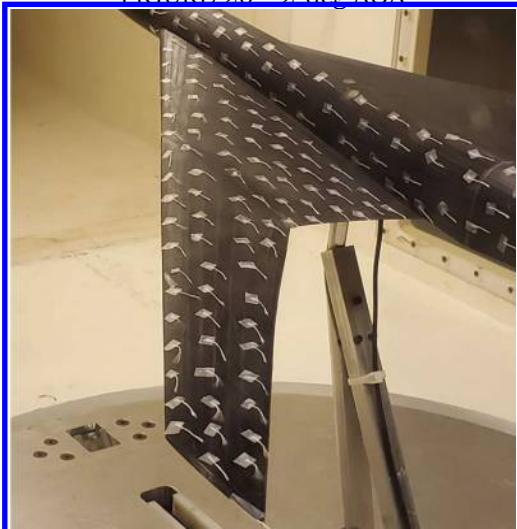FIGURE 21 – 6-deg AOA

FIGURE 22 – 11-deg AOA

D. Flow Visualization Shows Attached Flow at the Design Point, Transitioning to Vortically Dominant Flow at Higher Angles of Attack

We noticed previously that the aircraft develops sharply unfavorable pitching moment characteristics around α=6-deg but from the wind tunnel model we observe another interesting phenomenon around this angle of attack. At this angle the flow around the wind tunnel model begins to separate at the leading edge causing turbulent vortices to flow over the wing surface. Compare FIGURE 20 to FIGURE 21; to observe the activity in the in the small tufts placed along the surface of the wing. Note that FIGURE 20 is at α=2-deg and the flow is fully attached but in FIGURE 21 the model is at α=6-deg and the flow begins to separate; see the blurred tufts particularly near the trailing edge of the wing at the wingtip.

Even though at α=6-deg the wing has essentially stalled, the lift curve does not drop off like a classical stall event would indicate. That is because this wing planform has the ability to generate a good amount of vortex lift even after flow separation has set in. Recall that the planform of this wing is highly swept and features a large Yehudi which in some ways makes this platform not so different from that of a delta wing aircraft (i.e. Concorde) which are notorious for having excellent vortex lift characteristics.

In FIGURE 21 we observe the early onset of the flow separation at the leading edge of the wing but in this case the separation is mostly isolated to the tip region of the wing. The realization that wing is stalling first at the tip provides a solid explanation for the stability break noticed earlier in this paper.

Once again, the lift curve slope of this airplane indicates no sudden decrease in lift all the way up to at α=22-deg. In FIGURE 22 the model is set to at α=11-deg where the separation of the flow is far more pronounced across a higher percentage of the planform. By this point the flow separation has progressed inward form the tip to the rest of the wing but is still overcome by the effects of vortex lift.

VI.   High Speed Volume Grid CFD Results

A.   Transonic Solutions Highlight the Need to Consider the Lower-Critical-Mach-Number

To this point we have predicted that the design of this supersonic aircraft will likely be tied to the Lower-Critical-Mach-Number which we have predicted to fall right around M~0.89. If this holds then we would expect to see no visible shock waves along the planform in any CFD solution run with a Mach number less than M~ 0.89. To test this the SU2 run was performed at the design angle of attack (α=0.2-deg) at a Mach number of M~ 0.87. FIGURES 23 and 24 show the relevant pressure

14

coefficient and Mach number contours for the upper surface of the planform. Taking a look at these figures there are in fact no visible shock waves impinging on any part of the wing planform. We've established that the aircraft is shock-free just below our predicted Lower-Critical-Mach-Number but now we want to see what happens if we slightly exceed this predicted Mach number but still maintain subsonic freestream flow.

FIGUREs 25 and 26 show the relevant contours for the airplane at a free stream Mach number of 0.95. What we notice here is that there is a very distinct shock wave being formed at the side of body around 80% of the root chord. This results provides some validity to the claim that the Lower-Critical-Mach-Number will wreak havoc in supersonic design problems.

Recall that the Mach cone angle, θ (also shown in EQUATION 8) for freestream flow that is sonic (M = 1.0) is a 90-degree angle. Technically, at a freestream Mach number of 0.95 there shouldn't even be a Mach cone but since the flow upstream of the shock is noticeably supersonic, there is in fact a Mach cone angle associated with this region of flow. The flow in this region reaches Mach 1.18 and the associated Mach cone angle is about 58-degrees, but the measured angle of the shock wave does not line up with that as seen in FIGURE 26 where it's measured to actually be about 65.8-degrees.

$$\theta = \sin^{-1}\left(\frac{1}{M_\infty}\right) \quad\quad [8]$$

This finding is curious but what is more interesting is that the shockwave does appear to be forming at the point on the fuselage where the second derivative of the cross-sectional area is maximized in accordance with the cutting plane for a freestream Mach number of around 1.0 (90-degrees). FIGURE 27 (overleaf) shows the superposition of the cross-sectional area curve with one of the isobars from the M=0.95 case but keep in mind that the cross-sectional area plot is upside down. We can see that the shock wave does indeed form at the point where the curve of the second derivative is maximized. The second derivate is calculated via sufficiently accurate finite differencing schemes.

The implications of this finding are that the formation of the shock wave may as well be rooted in the interaction of the fuselage geometry with the wing geometry as well as the principles of the Lower-Critical-Mach-Number.
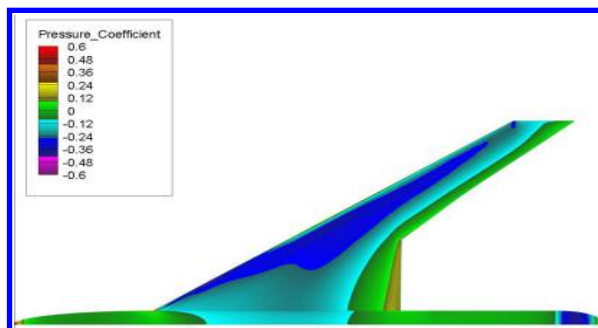

FIGURE 23. Pressure Coefficient Contour from *SU2* at Mach 0.87 (α = 0.2-deg, C_L = 0.178)

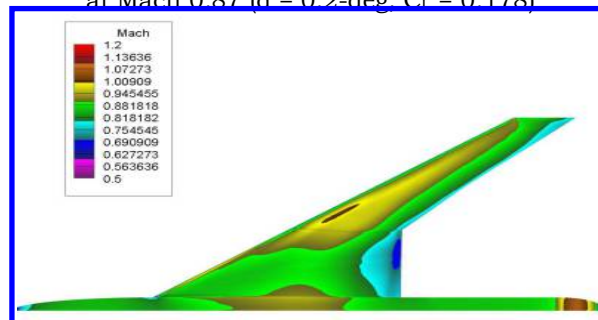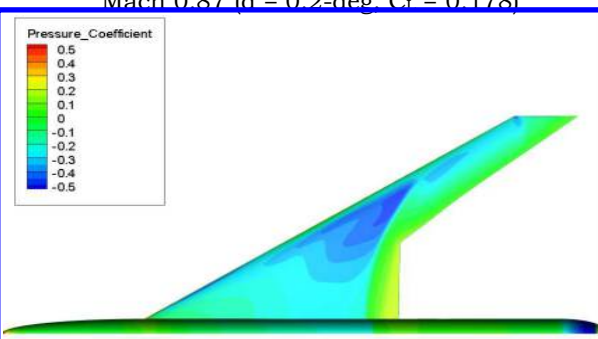FIGURE 24. Mach Number Contour from *SU2* at Mach 0.87 (α = 0.2-deg, C_L = 0.178)

FIGURE 25. Pressure Coefficient Contour from *SU2* at Mach 0.95 (α = 0.2-deg, C_L = 0.204)
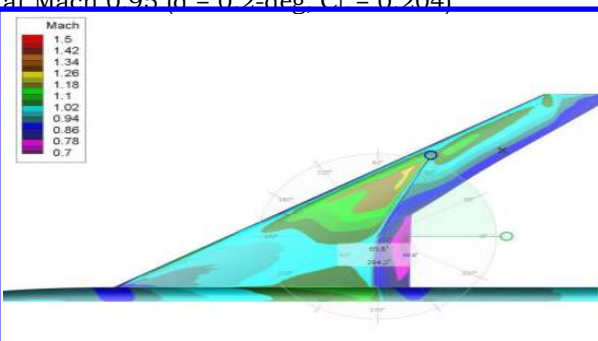

FIGURE 26. Shock Wave Angle Inconsistency with Mach Angle at Mach 0.95 (α = 0.2-deg, C_L = 0.204)
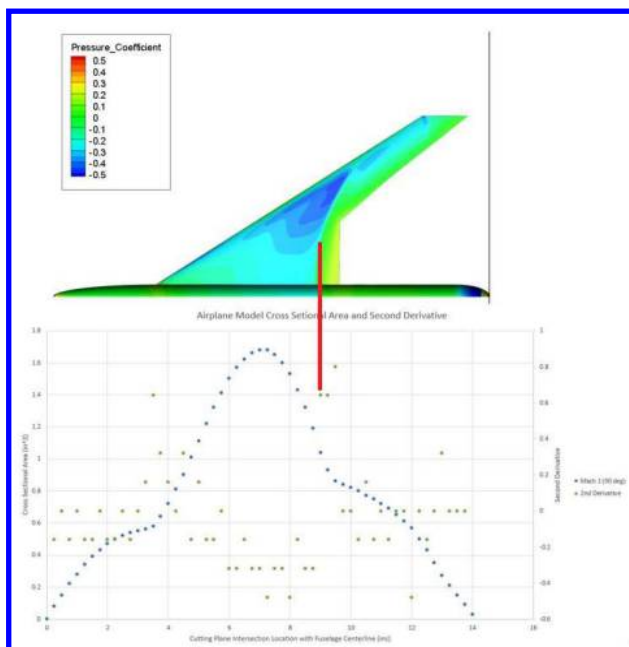
15

FIGURE 27. Pressure Coefficient Isobar Superimposed with the Cross-Sectional Area Distribution and it's Second Derivative (Mach 0.95)
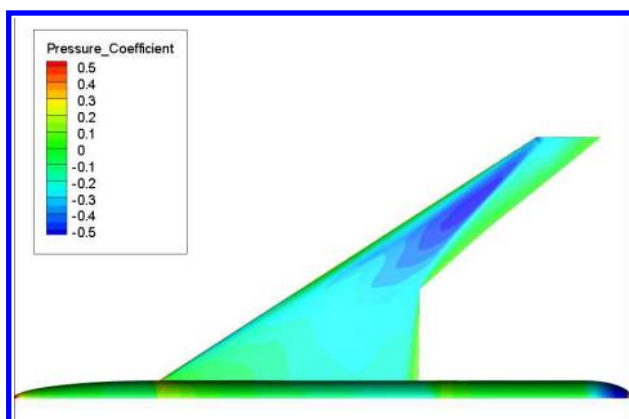

FIGURE 28. Pressure Coefficient Contour from *SU2* at Mach 1.05 (α = 0.2-deg. C_L = 0.186)

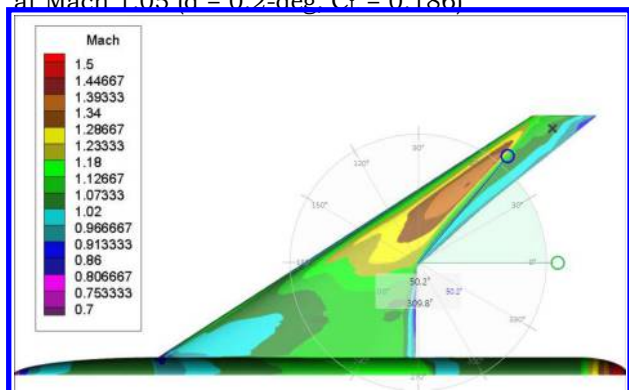FIGURE 29. Shock Wave Angle Inconsistency with Mach Angle at Mach 1.05 (α = 0.2-deg, C_L = 0.186

A further reading of Neumark [12] explains that this relatively strong shock wave is related to the aircraft exceeding its Lower-Critical-Mach-Number; that related to $Cp*$ for the unswept isobar lines near the wing-fuselage junction. Turn once again to TABLE 1 and refer to the M=0.95 values. At this freestream speed, $Cp*$ for an unswept isobar line is -0.09; $Cp*$ for a 57-degree swept isobar line is -0.58. Indeed, we see $Cpmin$ << -0.09 at the wing body junction where the shock forms. If we return to the low-speed solution (see FIGURE 15) we may not that the unswept isobar $Cpmin$ point is found proximate to the location where the wing/body junction shockwave forms. Recall that following Neumark's rules, we estimate the Lower Critical Mach of this configuration at M~0.89 and indeed flight at M=0.95 displays shockwaves even though we designed the swept wing to operate under sub-critical conditions.

B.   Supersonic Solutions Show the Impact of a Supersonic Trailing Edge

Next, let us look to FIGUREs 28 and 29 which show the relevant contours for the Mach 1.05 solution. The wing/body once again displays a prominent shock structure. We first note an unswept shock that seems to form right at the trailing edge of the wing at the wing/body junction. We also see a swept shock, swept back at ~50-degrees, forms outboard on the wing. Note that the Mach cone angle for this solution would be about 72.2-degrees (associated with 18-degrees of apparent sweep).

If we look at FIGURE 30, (overleaf) which is a counterpart to FIGURE 27, we see once again that the shock wave in question is being formed again at the point along the root chord where the cross-sectional area's second derivative is large. Since the Mach cone angle in this case is 72.2-degrees, then the cross-sectional area cutting planes according to Harris [19] need to be set to this same angle.

Recall, the Lower-Critical-Mach-Number was predicted to be M~0.89 so that it entirely expected that the interaction of the fuselages cross sectional area causing a blockage to increase the local flow speeds around the wing and thus triggering a shock wave; these qualitative expectations are supported by our findings using *SU2*.

In FIGURE 31 (overleaf), we can look at how the zero-lift drag changes with Mach number. We see that the zero-lift drag is heavily dependent on Mach number and increases sharply around
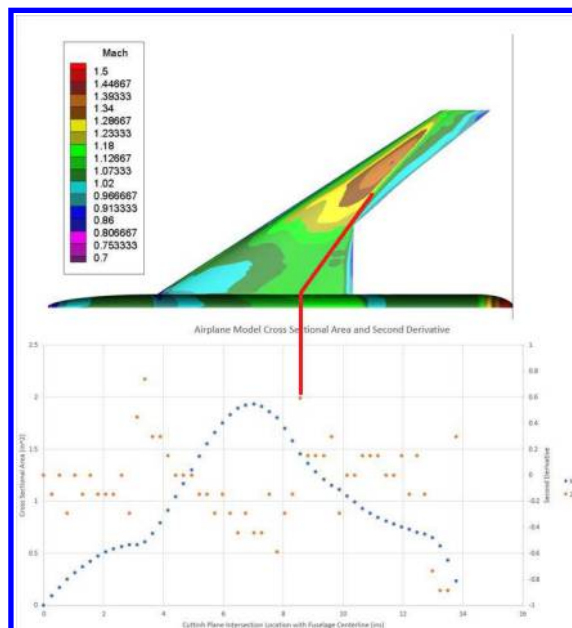
16

FIGURE 30. Pressure Coefficient Isobar Superimposed with the Cross-Sectional Area Distribution and it's Second Derivative (Mach 1.05)
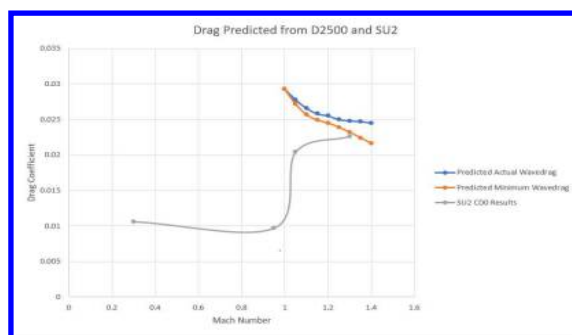

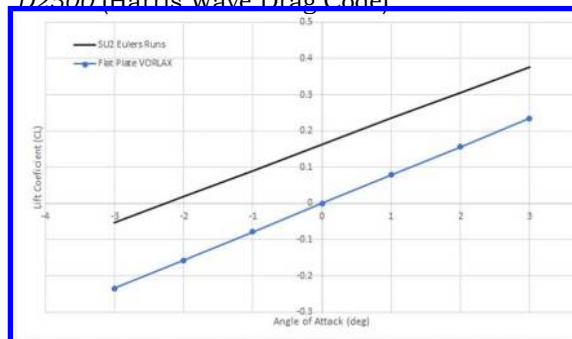FIGURE 31. Drag Predictions from *SU2* and *D2500* (Harris Wave Drag Code)

FIGURE 32. C_L vs α Plot at *M*=1.3 Cruise Speed – *VORLAX* and *SU2*

Mach 1.0, which is consistent with accepted classical aerodynamics. The Harris Wavedrag results are also superimposed on this figure. We can see that the drag results are largely similar in magnitude but not really of similar trend.

C. Mach 1.3 Design Point Solutions

The *SU2* solutions reveal that once again shocks dominate the flow. Flight at Mach 1.3 is expected to be above both the Lower-Critical (M~0.89) and Upper-Critical-Mach-Number (M~1.15).

In FIGURE 32, we see that slope of the lift coefficient is captured well between SU2 and VORLAX. As expected, the uncambered model has a substantial offset. What is promising here is that the SU2 model develops the target CL (CL~0.21) at approximately the angle-of-attack (a~+0.5-deg) we expected it to during the low-speed Potential Flow design process.

FIGURE 33 is a plot of normalized drag coefficients (CD-CD0) for both VORLAX and SU2. Once again we see that SU2 closely matches the VORLAX flat plate model with 50% analytical leading edge suction correction that we "calibrated" in our low-speed study.

Finally, FIGURE 34 reveals that VORLAX properly captures the longitudinal stability of the wing body. Both solutions show stable flight over a range of *CL*.
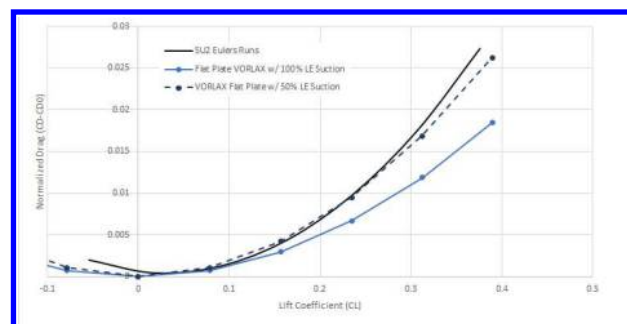

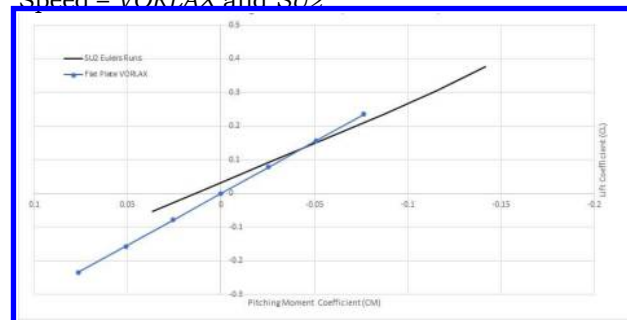FIGURE 33. C_L vs CD-CD0 Plot at *M*=1.3 Cruise Speed – *VORLAX* and *SU2*

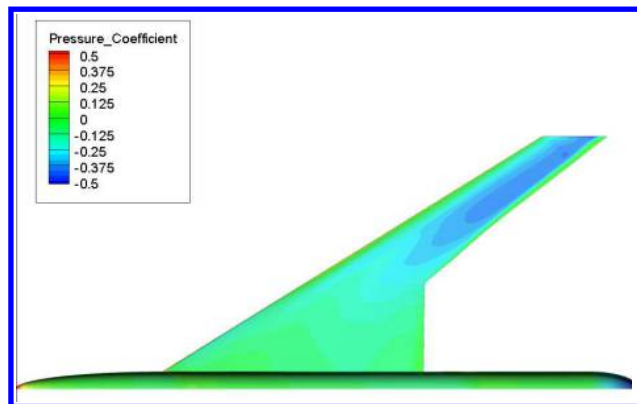FIGURE 34. C_L vs Cm Plot at *M*=1.3 Cruise Speed – *VORLAX* and *SU2*

17

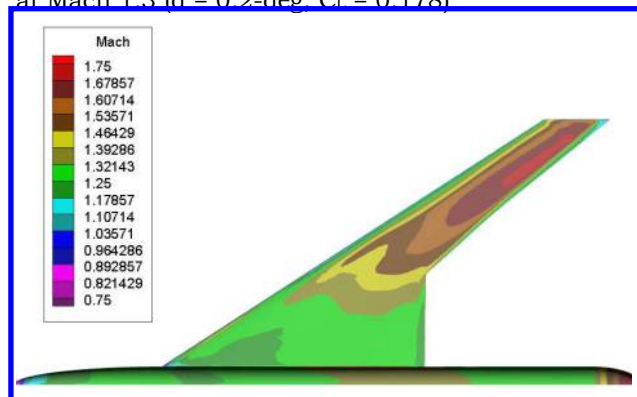FIGURE 35. Pressure Coefficient Contour from *SU2* at Mach 1.3 (α = 0.2-deg, C_L = 0.178)

FIGURE 36. Mach Number Contour from *SU2* at Mach 1.3 (α = 0.2-deg, C_L = 0.178)
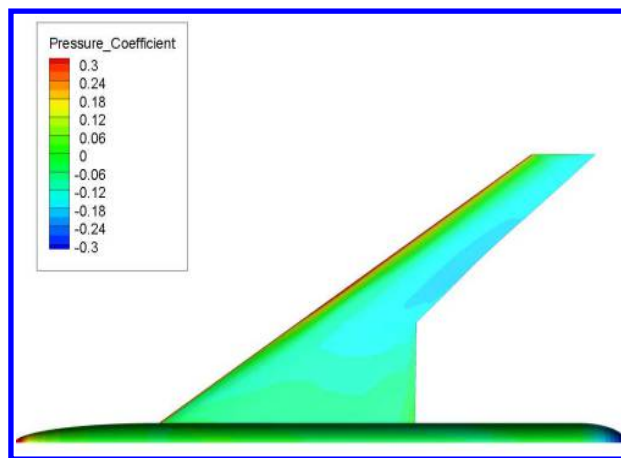Cruise Speed – *VORLAX* and *SU2*

FIGURE 37. Pressure Coefficient Contour from *SU2* at Mach 2.0 (α = 0.2-deg, C_L = 0.110)

FIGURE 35 shows the pressure coefficient contours for the wing at Mach 1.3. We observe a very strong shock wave forming at the trailing edge of the planform. FIGURE 36 shows this same contour but instead in terms of local Mach number and at the location of the pressure discontinuity, the flow suddenly slows down from about Mach 1.7 to about Mach 1.2. The lift coefficient produced here is 0.178 which is actually slightly lower than the predicted and required 0.21, but this pesky shock wave is certainly responsible for some of the loss of lift at the design speed.

D.   **Mach 2.0 Overspeed Solutions**

The trend seen in the *SU2* results so far is that a prominent shock wave forms for flight just above the Lower-Critical-Mach-Number and then "morphs" and becomes less prominent as Mach number increases. Following this trend, it is not a bad assumption to assume that if the Mach number were to continue increasing that the shock might "fall off" the wing altogether and finally leaves us with a shock-free planform. Out of pure curiosity we ran this wing through a Mach 2.0 simulation which is much faster than it was ever designed for to see if a shock would still be visible. FIGURE 37 shows that the trend is actually correct and the shock wave that has been evident this far has "fallen off" the wing planform. What shock waves exist are either detached or aligned to the wing leading and/or trailing edges.

VII.   Schlichting's Observation Regarding Subsonic or Supersonic Trailing Edge Flow

We believe that something else may be going on here beyond a literal reading of Küchemann [5] and Neumark; [12] this is hinted at in Schlichting. [20] Our planform was chosen with great attention to the *Cp** implications of its leading-edge sweep angle but without any attention to its trailing-edge sweep angle; those were chosen to facilitate the elliptical span load, and promote stable stall characteristics as well as to provide for room for landing-gear and high-lift-system integration. Schlichting asserts that the sweep angle of the trailing edge might be just as important in deciding the Lower-Critical-Mach-Number. [20]
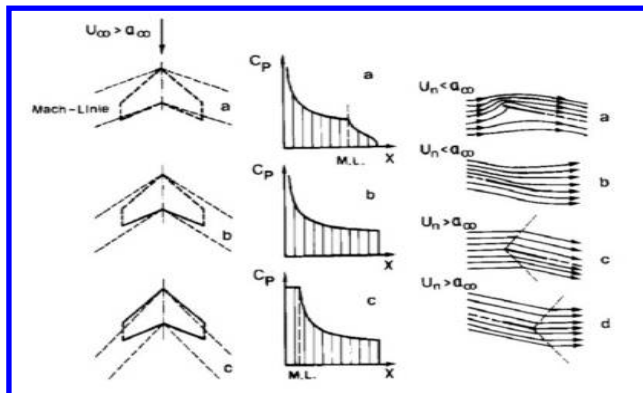
18

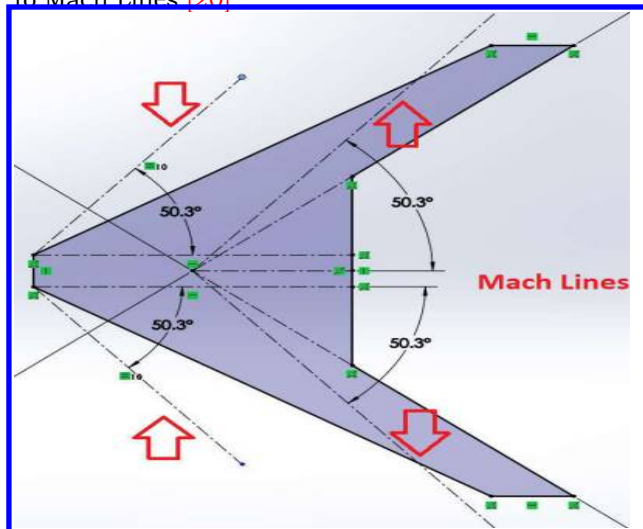FIGURE 38. Implications of Sweep Angles in Relation to Mach Lines [20]

FIGURE 39. Wing Geometry Superimposed on Mach Cone Angles at Mach 1.3 (Mach Lines Propagate from Trailing Edge Intersection)
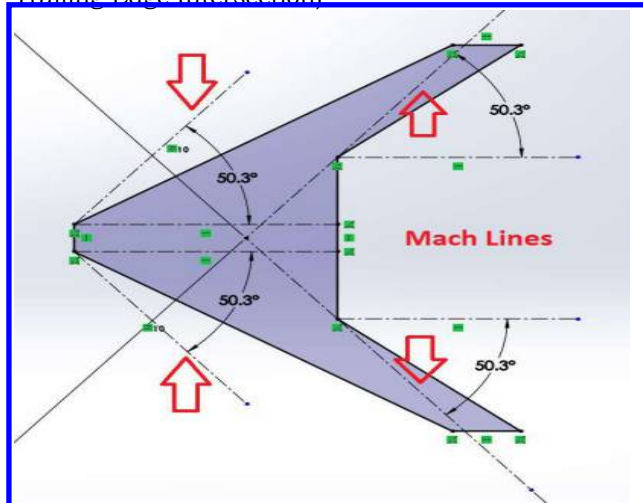

FIGURE 40. Wing Geometry Superimposed on Mach Cone Angles at Mach 1.3 (Mach Lines Propagate from Yehudi Intersection)

FIGURE 38 (case "a") shows the potential implications of the wing geometry [20]. It illustrates a wing whose leading edge is swept behind the Mach line generated by the incoming flow but whose trailing edge is not thus triggering a trailing edge shock wave. In the case of our design, the outboard trailing edge has a significantly shallower sweep angle (48.7-deg) while the trailing edge in the "Yehudi" is completely unswept.

FIGURE 39 shows FIGURE 38(a) recreated for this specific wing and with Mach angles that correspond to the upper design point of Mach 1.3 (50.3-degree Mach cone angle). If the Mach lines at this Mach number are superimposed against the wing planform, we see that the wing does in fact replicate the situation seen in FIGURE 38(a) – it has a subsonic leading edge and a supersonic trailing edge; thus shocks emanating aligned with the Mach cone interact with platform of the wing.

In FIGURE 40 we show the same concept, but the Mach lines instead radiate out from the end of the Yehudi and extend into the side of body. The lines seen in FIGURE 40 show a keen resemblance to the results from *SU2* in FIGUREs 28, 29 and 30 but the inconsistency is that those runs were at Mach 1.05 in which case the shock angle should have had a much different angle than what we actually see. We expected to see FIGURE 35 resembling FIGUREs 39 and 40 since those were the runs at Mach 1.3 where the Mach cone angle would match, but we do not observe much similarity between these sets of figures presumably because Mach 1.3 exceeds the Upper-Critical-Mach-Number of the wing.

VIII. Reconsidering the Low-Speed Design Process to Consider the Sweep of All Isobar Lines

These results point to the concept of the Lower-Critical-Mach-Number coming into play, because for both of the workups provided in FIGUREs 39 and 40, they were given a sweep angle equal to the leading-edge sweep of 57-degrees. But as Neumark [12] has previously been cited saying, it all depends on the sweep angle of the local pressure isobars. So really, it's not totally accurate to assume that we can use 57-degrees in the previous workup, instead we might try to use the sweep of the local isobars which would have the effect of decreasing the critical pressure coefficients.

19

This becomes a circular problem in a sense because once a shock has formed, it will fundamentally change the wings pressure distribution and thus the wings pressure isobar pattern. Luckily, we can assume that the pressure isobar pattern will remain similar in shape (but different in magnitude) up until the point of a shock formation, meaning we can use the low-speed isobar pattern to determine local sweep angles.

Starting with the Mach 0.95 case, we have observed that there is a shock forming in the presence of a most negative pressure coefficient of -0.48. Instead of solving the difficult problem of iterating through sweep angles to find a critical isobar sweep angle, we can instead visually obtain the isobar sweep angle from FIGURE 41 in the region where the Mach 0.95 shock is forming and extrapolate from there. We see that the low-speed isobar sweep in the region where the shock forms was ~25-degrees. Interestingly enough, this isobar sweep angle is actually pretty similar to the shock wave angle measured in terms of sweep from vertical, instead of the angle from horizontal in the case of the Mach cone angle. We can then return to TABLEs 1 and 2 to consider the critical pressure coefficient for M=0.95 flight @ 25-degrees sweep; we find $Cp*$~-0.23 and $Cp0*$ ~ -0.12. The theoretical "shoe-seems-to-fit" our solution once again as the low-speed solution in the vicinity of the shock formation exhibits $Cpmin$~-0.2; which is much less than the predicted critical limit to be not less than -0.12. The high-speed solution features suction pressures with $Cpmin$ in the -0.3 to -0.4 region just ahead of the shock; this too is consistent with $Cp*$~-0.23;

Let us continue with the Mach 1.05 solution. Once again, the first step is to get a measure of the local isobar pattern sweep angle out at the point where the shock wave is visually forming in the Mach 1.05 *SU2* solution. This is shown below in FIGURE 42 and reveals a much more drastic sweep angle of about 50-degrees. Returning once again to TABLEs 1 and 2 to consider the critical pressure coefficient for M=1.05 and 50-degrees sweep; we find $Cp*$~-0.37 and $Cp0*$~-0.27. Here the correlation is weaker. We see that the local low speed pressure coefficient in the region of the shock is only -0.21 in the most intense areas of suction. However, the Mach 1.05 case does exceed $Cp*$ with a $Cpmin$ ~ *-0.53* upstream of the shock. Thus, Neumark and Küchemann's methods only seem to work in retrospect with the airplane flying with a partially supersonic trailing edge.
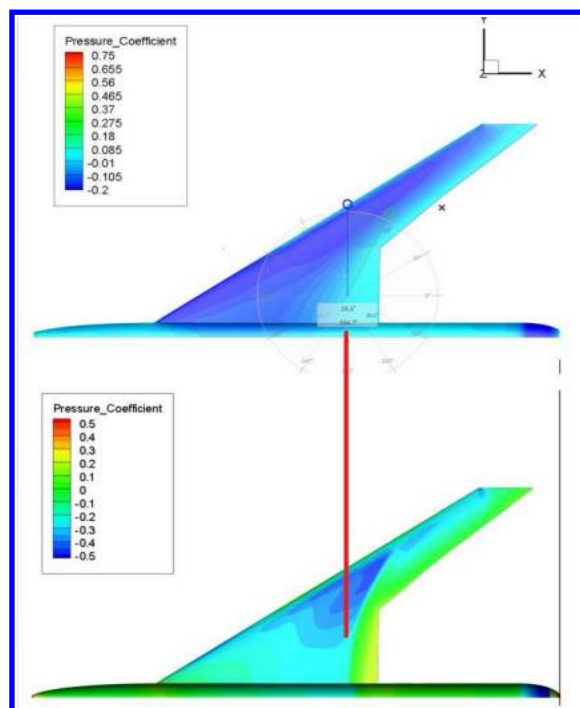

FIGURE 41. Local Isobar Sweep Angle from the Low Speed *SU2* Solution Superimposed on the Relevant Mach 0.95 *SU2* Solution
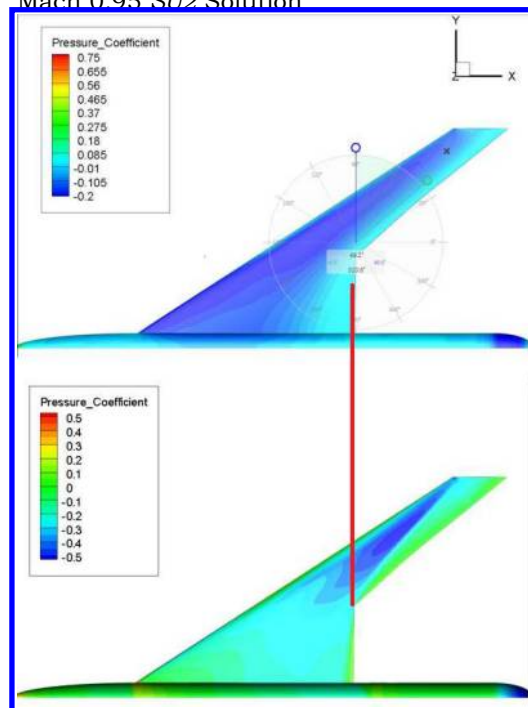

FIGURE 42. Local Isobar Sweep Angle from the Low Speed *SU2* Solution Superimposed on the Relevant Mach 1.05 *SU2* Solution

20

IX.   Conclusions

We used an admittedly simple, potential flow code, to design a supersonic cruise wing. In retrospect, the wing encountered some design issues due to misunderstandings regarding the governing aerodynamic rules.

The good news was that the upper surface isobar patterns synthesized using VORLAX "sandwich panels" closely matched the volume grid SU2 results at low speeds. Wind tunnel testing confirmed fully attached flow around the design angle-of-attack and confirmed that the wing developed its intended *CL* at these conditions. We also confirmed that we could design a wing that achieved an elliptical transverse span loading; this should be good for induced drag. The bad news is that these wings seem to follow induced drag trends across a wide range of Mach numbers indicative of a greatly diminished leading-edge suction effect, all despite having blunt leading edge airfoils.

We learned that any low-speed *Cp0** we compute must be estimated using Küchemann's swept wing Cp* equation and "corrected" back to low Mach number conditions using the Prandtl-Glauert rule keyed to the characteristic sweep angle.

We learned that shock waves seem to follow Neumark's rules. Any bi-laterally symmetric wing/body will develop isobar patterns that unsweep completely across the centerline and unsweep partially on the planform near the side of body. By definition, such a shape will always have a Lower-Critical-Mach-Number less than sonic. Once the Lower-Critical-Mach-Number has been exceeded, a shock wave will form and "contaminate" flow over the wing.

We think that we can predict the Lower-Critical-Mach-Number of a wing-body configuration reliably from low-speed pressure isobar plots; we confirmed this after generating a shock-free SU2 solution at *M*=0.87 and a second solution with a prominent body-induced shock at *M*=0.95.

Our planform incorporated an unswept trailing edge which was driven by the need for landing-gear and high-lift-system integration. However, this planform was bad for supersonic aerodynamics because it led to the wing pressure profiles associated with a subsonic-leading-edge but supersonic-trailing-edge. This design, according to Schlichting, forces a prominent and inevitable mid-chord shock wave.

In this paper we also explored how the proverbial "Mach Cone Angle" played into the formation of the shock waves the angles thereof. In this we found inconsistencies between the local Mach numbers and the angles that the shockwaves propagated along the planform. By and large we were unable to reconcile these discrepancies.

Although we placed strong emphasis that the shockwaves discovered we triggered by exceedance of our Lower-Critical-Mach-number, we also explored implications of wing-body cross sectional area blockages. We found that the shockwaves were all triggered at the fuselage station that aligned with the largest second derivative in cross sectional area. The cutting planes proposed by Harris in the construction of the cross-sectional area plots was found to be valid and accurately predicted shockwave locations, but this is more of an auxiliary finding to the principles of the Lower-Critical-Mach-Number.

If we were to revisit this, we'd likely attempt to design a different planform all together. Taking the Küchemann, Neumark and Schlichting methods into consideration we would pay more attention to the sweeps of the developed isobar pattern, not to the LE or TE sweep of the wing.

Acknowledgements

X.   References

1. Kurus, N.J., et.al., "Final Design of a Transatlantic Supersonic Transport Aircraft," Senior Capstone Design Report, AEE 468, Arizona State University, 2019.
2. Kurus, N.J., "Unique Design Discoveries for a Modern Mach 1.3 Airliner including Anomalies in the Shock Wave Formation along a High Swept Blunt Leading Edge Wing," M.S. Thesis, Aerospace Engineering, Arizona State University, November 2020.
3. Anonymous. "Concorde". https://en.wikipedia.org/wiki/Concorde.
4. Kurus, N.J. and Takahashi, T.T. "Aerodynamic Design Challenges of a Mach 1.3 Supersonic Airliner Concept," AIAA 2021-0591, 2021.
5. Küchemann, D., *The Aerodynamic Design of Aircraft*, AIAA, Virginia, 2012, Chaps. 4, 5.
6. Busemann, D., "Aerodynamischer Auftrieb bei Uberschallgeschwindigkeiten." Proceedings, Volta Congress. Reale Accademia d'Italia. 1935.
7. Ludweig, H., "Pfeilfltigeln bei hohen Geschwindigkeiten." Lilienthal-Gesellschaft. Bericht 127, 1940, p. 44.
8. Jones, R.T., "Thin Oblique Airfoils at Supersonic Speed." NACA. TN 1107. 1946.
9. Jones, R.T., "Wing Planforms for High Speed Flight," NACA TR 863, 1946.
10. Kirkman, J.J. & Takahashi, T.T., "Revisiting the Transonic Similarity Rule: Critical Mach Number Prediction Using Potential Flow Solutions," AIAA 2016-4329, 2016.
11. Kirkman, J.J. & Takahashi, T.T., "Critical Mach Number Prediction on Swept Wings," AIAA 2017-0266, 2017.
12. Neumark, S., "Critical Mach Numbers for Thin Untapered Swept Wings at Zero Incidence," ARC R&M 2821, 1954.
13. Nicolai, L., *Fundamentals of Aircraft Design*, METS Inc., San Jose, CA, 1975/1984.
14. Raymer, D., Aircraft Design: A Conceptual Approach, AIAA, 2018.
15. Miranda, L. R., Baker, R. D., and Elliott, W. M., "A Generalized Vortex Lattice Method for Subsonic and Supersonic Flow," NASA CR 2875, 1977.
16. Obert, E., *Aerodynamic Design of Transport Aircraft*, IOS Press, Delft, 2009.
17. Peristy, L.H,. Perez, R E., Asghar, A.& Allan, W.D.E., Reynolds Number Effect of Leading Edge Tubercles on Airfoil Aerodynamics, AIAA-2016-3260, 2016
18. Pope, A. & Harper, J., *Low-Speed Wind Tunnel Testing*, 2nd Edition, Wiley, New York, 1966
19. Harris, R.V., Jr., "An Analysis and Correlation of Aircraft Wave Drag," NASA TM X-947, 1964
20. Schlichting, H., & Truckenbrodt, E., *Aerodynamics of the Airplane*, McGraw Hill, New York, 1979.